DIRECT TRANSITION TO TURBULENCE IN A 3D BOUNDARY LAYER

Viaud B* , Serre E , Chomaz JM*****
Centre de recherche de l'armée de l'air (CReA) BA 701 F-13661 Salon de Provence,
****Laboratoire M2P2 CNRS Universités Aix-Marseille IMT Chateau-Gombert F-13451 Marseille,***
*****Laboratoire d'hydrodynamique (LadHyX) CNRS Ecole Polytechnique F-91128 Palaiseau***

Keywords: *boundary layer, transition, global mode*

Abstract

The transition to turbulence process in a rotating boundary layer is numerically investigated. In particular we will show that, when the Reynolds number based on the forced throughflow is increased above a threshold value, an impulsive perturbation gives birth to a self-sustained saturated wave which caracteristics identify as a global elephant *mode as described by [1]. This saturated wave is itself absolutely unstable with zero Floquet number, and this secondary instability leads to a very unorganized state, which can be labelled as incipient turbulence. This scenario relies on low incoming noise upstream of the primary front, and a sufficiently strong impulsive perturbation as the first global bifurcation is known to be subcritical [2]. For the first time it confirms the possibility of a direct transition to turbulence through the elephant cascade.*

1 Introduction

The flow encountered above an infinite rotating disk is an academic example of three dimensional boundary layers, and is used to examplifie the crossflow instability of inflexional velocity profiles. When a second rotating disk is added parallel to the first one, the configuration models, for example, the cavity between the disks holding the blades of a turbine or compressor. Moreover the presence in the boundary layer of both azimuthal flow and radial crossflow makes its stability properties similar to those of swept wing boundary layers. For infinite disks in rotor-stator configuration, the theoretical analysis of the laminar flow has been done by [3], and [4]. For co-rotating disks of finite extent with a forced inflow, early results were obtained by [5] who made an experimental and analytical investigation. He showed that the base flow is made of four parts: an inflow and an outflow zones framing a quasi-solid-body rotating core sandwiched by two thin Ekman boundary layers. Later work by [6] have confirmed these results for the stationary flow, and added measurements of Ekman-layers instabilities. A review of the subject can be found in [7]. As for the transitional régime, recent numerical work by [2] has demonstrated the similarity between the flow over a single rotating disk, and the boundary layer encountered at the wall in an annular cavity with a forced radial inflow. The local stability properties of the velocity profiles were found to be the same, as soon as the boundary layer thickness is small compared to the gap. The global instability was shown to be subcritical, which accomodates both the linear results of [8] and the nonlinear dynamics proposed by [9]. Linear stability analysis has revealed that the flow above the single infinite rotating disk is subject to two generic types of instability. An inviscid instability, due to the inflexional nature of the velocity profile, is labelled type I, whereas type II is due to the combined action of viscous and Coriolis effects. Early results were obtanined by [10] and a recent review can be found in [11].

As far as the single disk is concerned, the matter of the transition scenario is currently much debated. This debate began with the discovery [12] that the type I inflexional instability undergoes a transition from convective to absolute behaviour at a Reynolds number just below the value repeatedly found for transition to turbulence in the experiments. Nevertheless [8] argued that when non-parallel effects are taken into account the flow is linearly globally stable. A later study by [13] showed how, in the context of a model equation, detuning arising from the radial variation of absolute frequency might be stabilizing enough to enforce linear global stability over absolute instability. However, nonlinearities can counterbalance this stabilizing effect when they are present, and lead to a nonlinear global mode, even in the case of linear global stability [14]. In this case, the presence of an absolutely unstable region of finite extent is a sufficient condition for the existence of a nonlinear global mode, which for weakly non-parallel flows, takes the form of a steep front located at the position of transition from convective to absolute instability and separating upstream evanescent perturbations from a downstream saturated wave. This mode was first described in [15]. This opened the possibility for a direct route toward turbulence, and further investigations were made by [9]. This author proposed that an *elephant* nonlinear global mode develops as a consequence of the absolute instability, and investigated the local stability of the saturated type I wave that should be present downstream of the transition point between convective and absolute instability. This nonlinear wave proved to be itself absolutely unstable as soon as it formed, adding credit to the direct route scenario. Still the existence of the primary nonlinear global mode had not been confirmed.

For the particular case of the rotating cavity with throughflow, we have shown the existence of a subcritical global bifurcation toward an elephant mode of azimuthal wave number 68, nonlinearities compensating the stabilizing effect of non-parallelism. The present paper further adresses the question of the stability of the resulting saturated wave with respect to secondary perturbations. In this prospect, the computational domain downstream of the front has to be long enough to feed a would-be secondary front. Moreover, some computations have been performed in a cavity of angular extent $2\pi/68$, thus enforcing the sole computation of mode number 68 and its harmonics.

The configuration is detailed in §2, which highlights in which way it differs from the well-documented single disk case. Section 3 presents the numerical method, with particular stress on key points such as boundary conditions, artificial selective damping and how local stability analysis is conducted. Primary instability, in the form of a steep fronted global mode, and secondary instability are the subject of §4. The competition between this mechanism and other routes to turbulence is further discussed in §5.

2 Configuration

The incompressible fluid motion is governed by the Navier–stokes equations, written in the rotating frame, and with dimensional quantities stared.

The present configuration is made of two co-rotating disks of finite radial extent, having same axis and angular velocity ($\blacksquare_d^* = \Omega_d^* \mathbf{e}_z$). The cavity is open at both inner and outer radius, and a flow is forced at the hub which exits at the rim. The two disks are separated by a gap of height h^* and their radial extent goes from $R_{in}^* = R_2^*$ to $R_{out}^* = R_1^*$. As the gap h^* is large with respect to the Ekman boundary layer scale $\delta^* = \sqrt{\nu/\Omega_d^*}$ the flow at any radial station is made up of a core locally in solid body rotation between two thin Ekman layers. The mass flow rate Q^* is imposed at the hub through the use of Dirichlet boundary conditions on the velocity. Thus the geometry is defined by two control parameters, the curvature $R_m = (R_2^* + R_1^*)/\Delta R^*$ and aspect ratio $L = \Delta R^*/h^*$, while the flow itself is governed by two other global control parameters, the system rotation rate $\widetilde{\Omega^*}$ and the non-dimensional mass flow rate $C_w = Q^*/(\nu R_1^*)$, ν being the kinematic viscosity. The system rotation rate [12] is defined by $\widetilde{\Omega^*} = (\Omega_f^* + \Omega_d^*)/4 +$

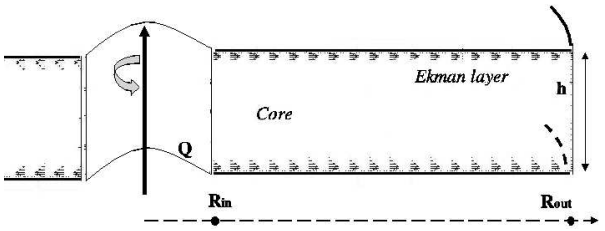

Fig. 1 Sketch of the annular cavity. Velocity vector field in the (r,z)-plane depicts the radial base flow.

$\sqrt{((\Omega_f^*+\Omega_d^*)/4)^2+(\Delta\Omega^*)^2/2}$ where Ω_f^* is the fluid core rotation velocity and $\Delta\Omega^*=\Omega_f^*-\Omega_d^*$. The value of Ω_f^* is local and unknown, and therefore so is $\widetilde{\Omega^*}$.

In the limit of high rotation rates, Ekman's linearity assumption holds, as nonlinear effects are negligeable compared the Coriolis force, and an *asymptotic solution* for the flow in the cavity can be obtained by matching linear Ekman solutions for two single infinite disks. Such a matching had been suggested in [16], and was shown to describe accurately the flow for low values of C_w in [17]. Indeed, for high rotation rates (controled by $\widetilde{\Omega}$) the Coriolis effects are strong, whereas for high mass flow rates (controled by C_w) the advection terms are important (and so are the nonlinear effects). In the case of such a matched solution, the azimuthal component of the velocity in the core stands for the geostrophic velocity in the classical Ekman solution, and will be hereafter labelled V_g^* and keep the name of *geostrophic velocity*. A convenient global Reynolds number can be extracted from the ratio of the Ekman length scale ($\delta^*=\sqrt{\nu/\Omega_d^*}$) and the cavity height (h^*). The Reynolds number thus obtained, $Re_h=(\delta^*/h^*)^2$ has the advantage to represent the thinness of the boundary layer, and control the mean velocity gradient. Local stability properties are controled by local parameters, the Rossby number ($Ro=\Delta\Omega/\widetilde{\Omega}$) and the local Reynolds number ($Re_\delta=(V_g^*\delta^*)/\nu$). The Rossby number acts on the shape of the velocity profiles (which are subject to inflectional instability), and the local Reynolds number control the magnitude of the velocity, as it is proportional to the geostrophic velocity. The Rossby number influences the critical value of the Reynolds number Re_c, and so the stability condition $Re_\delta > Re_c$ depends on both local (Re_δ and Ro)control parameters. The system is made non-dimensional using the following scales for time, length, velocity, pressure and mass flow rate respectively:

$t_{ref}=\Omega_d^{*-1}$, $l_{ref}=h^*$, $V_{ref}=\Omega_d^* h^*$, $P_{ref}=\frac{1}{2}\rho^*\Omega_d^{*2}R_1^{*2}$, and $Q_{ref}=h^{*3}\Omega_d^*$.

The asymptotic solution for high rotation rates, written in the rotating frame of reference reads then:

$$\begin{aligned} u(r,z) &= -V_g(r)\left[\exp\left(-\tfrac{z+\frac{1}{2}}{\delta}\right)\sin\left(\tfrac{z+\frac{1}{2}}{\delta}\right)-\exp\left(\tfrac{z-\frac{1}{2}}{\delta}\right)\sin\left(\tfrac{z-\frac{1}{2}}{\delta}\right)\right] \\ v(r,z) &= V_g(r)\left[1-\exp\left(-\tfrac{z+\frac{1}{2}}{\delta}\right)\cos\left(\tfrac{z+\frac{1}{2}}{\delta}\right)-\exp\left(\tfrac{z-\frac{1}{2}}{\delta}\right)\cos\left(\tfrac{z-\frac{1}{2}}{\delta}\right)\right] \end{aligned}$$

Note that axial velocity in the core ($w(r,0)=\frac{\delta}{r}V_g(r)$) is proportional to δ/r and is asymptotically smaller than u or v, when δ/r goes to zero, which is why it is usually taken to be zero. The geostrophic velocity can then be obtained from this asymptotic solution through mass flow rate conservation:

$$Q=\int_{-1/2}^{1/2}2\pi r u(r,z)dz \Rightarrow V_g(r)=\frac{-Q}{2\pi r\delta}=\frac{-C_w\nu R_1}{2\pi r\delta} \qquad (1)$$

And the local control parameters can now be written explicitly:

$$Re_\delta=\frac{-V_g^*\delta^*}{\nu}=\frac{R_1C_w}{2\pi r} \qquad Ro=-\frac{Re_\delta}{r\sqrt{Re_h}} \qquad (2)$$

These analytical formulations are based on the asymptotic solution and give only approximate values of Re_δ and Ro when nonlinear effects become important. More accurate values were used in the course of our investigation, which were computed based on the nonlinear DNS solution. In this prospect the geostrophic velocity is measured in the midplane of the cavity, as well as the mass flow rate, and the Rossby number is computed following $Ro=V_g/r$ and the Reynolds number following $Re_\delta=-Ror\sqrt{Re_h}$.

This configuration differs from the single infinite rotating disk mainly because of the way local control parameters vary with r. Indeed, former investigations [2,] have shown that confinement does not affect local instability properties

compared to the single-disk case, when the two boundary layers are well separated. For the radial inhomogeneity one must note that for the single-disk case, the local Reynolds number increases outward like r, whereas here equation 2 shows that it decreases like $1/r$. Moreover, for the single-disk case, the Rossby number is chosen once and for all, and is a global control parameter. On the contrary, in the cavity configuration, the Rossby number is a local parameter, decreasing outward like $1/r^2$ and causing the critical Reynolds number Re_c associated to the different thresholds (convective instability, absolute instability, turbulence) to decrease faster than the actual local Reynolds number (Re_δ).

3 Numerics

3.1 Spatial and time discretizations

The numerical solution is based on a pseudospectral collocation-Tchebyshev method in the non-homogeneous radial and axial directions (r,z) and a Fourier-Galerkin method in the 2π - periodic tangential direction.. The Tchebyshev approximation is associated with Gauss-Lobatto collocation points $(\widehat{r}_i,\widehat{z}_j), k = 0,...,K-1$ and $m = 0,...,M-1$ defined in the square $[-1,1]$. The natural gathering of these points near the boundaries is well adapted to the description of the thin boundary layers which develop at the walls. Then, for each of the N Fourier modes, the solution $(\mathbf{U},p)$ is approximated by Tchebyshev polynomials of degree at most equal to $K-1$ in the radial direction and to $M-1$ in the axial direction. We note that $N/2$ is the cut off frequency of the Fourier series.
This pseudo-spectral discretization ensures exponential convergence of the solution, see [18].
Owing to the decomposition on a Fourier basis, it is straightforward to impose the chosen periodicity $\beta = 68$ in the azimuthal direction, by concentrating the mesh points in a sectorial cavity of angular extent $2\pi/68$. Some additionnal computations have been done using $\beta = 4$ to check that the obtained results were not dependent of the imposed periodicity.

The temporal discretization is a projection scheme, based on backwards differencing in time [18]. The projection scheme requires the solution of a pressure Poisson equation to (approximately) maintain solenoidality of the velocity.
The equations are discretized in time using a second-order semi-implicit scheme which combines an implicit treatment of the diffusive term and an explicit Adams-Bashforth extrapolation for the non-linear convective terms. The unsteady term is approximated by a second-order backward Euler finite-difference scheme. Its good stability properties for an advection-diffusion equation have been shown before by[19].
The computation of the non-linear terms is performed using a pseudo-spectral technique with calculations of the derivatives in each direction in the spectral space while the products are calculated in the physical space. A FFT algorithm is used to connect the spectral and the physical spaces. On the other hand, the implicit diffusive term is evaluated through spectral differentiation matrices.
Finally, each time step involves successive solution of three uncoupled Helmohltz equations for the pressure predictor, the velocity and the pressure corrector, respectively. A direct solver is used for each Fourier mode, based on the full diagonalization technique [18].

For a *long* cavity defined by $L = 10$ and $Rm = 5$, the number of points has been kept to 10 in the azimuthal direction. Resolution-test computations have been carried with twice as many points (20), and have demonstrated that solutions are strictly unaffected in the linear régime, and that the pic amplitude of the wave paquet vary by less than 5% in the nonlinear one. In the two inhomogeneous directions, the number of mesh points has been progressively increased up to a final size of 649×65 points in the radial and axial directions respectively. For the broad domain computations, discussed in section 5 and carried in a quarter of circle, the azimuthal number of point has ben set to 170. The associated time step was $\delta t = 2.10^{-5}$. The expected inertial range of the turbulent cascade has been estimated using measurements of the size and associated veloc-

ity of the primary rolls (corresponding to type I saturated vortices of the primary global mode), and an estimate of the Kolmogorov length scale has been done for this particular flow. Based on this estimate the resolution of the final mesh is approximately ten Kolmogorov length scales at its coarsest in the radial direction, and approximately six Kolmogorov length scales at its coarsest in the axial direction.

As the base flow is symmetric with respect to the plane at mid-height, and the gap between the disks is large enough to prevent any confinement effect, computational effort has been spared by reducing the computed domain to the upper half of the cavity ($z \in [0;1/2]$), thus simulating a single boundary layer. This reduction of the computational domain has been extensively validated in shorter cavities, by comparison between simulations ran in full and half cavities.

3.2 Boundary conditions

At the disk, usual no-slip boundary conditions are applied, and stress-free conditions at the lower plane, enforcing the symmetry with respect to the middle of the cavity.

At the outflow, convective boundary conditions (Sommerfeld type) were used in order to prohibit reflections of the wave packets. Such conditions implemented through a local explicit discretization with a constant advection velocity proved to be best suited here [2]. So at each time step $n+1$ the three components imposed at the outflow are updated following the equation $u_j^{n+1} = u_j^n - C\frac{\delta t}{\delta r}(u_j^n - u_{j-1}^n)$ where C is the chosen outlet convection velocity.

At the inflow, pre-computed velocity profiles, picked up from the computations of the axisymmetric flow in a shifted cavity overlapping the present one were imposed [2]. This inlet boundary condition imposes a balanced flow matching the nonlinear subsequent base flow and forces the desired mass flow rate. If the usual Poiseuil profile were imposed at the inlet, it would produce an entry zone preceeding the establishment of the Ekman layer, as shown by [5], wich may be unstable [20] and contaminate the the rest of the flow. Nevertheless, very slight imperfections in the imposed velocity profiles are at the origin of amplified convective axisymmetric type II rolls. These are known to be convective and leave the cavity. But, even for very low initial amplitude, exponential growth occuring during the transit through a long cavity may lead them to finite amplitude before reaching the outflow. So that a filtering or damping have to be applied to prevent them from modifying the intrinsic dynamics of the downwind half of the cavity. Being axisymmetric they cannot be filtered in the azimuthal direction, and a frequency criteria must be chosen. A buffer zone is placed at the inlet, where possible oscillations of the zero azimuthal wave number are damped using the selective frequency damping, as proposed by [21].

3.3 Local analysis

The DNS code can be used to conduct a local stability analysis, following the method proposed by [22]. Toward this end, velocity profiles corresponding to any chosen radial position can be extracted from the converged mean flow, and extended to the whole radial extent of the computational domain to create a new strictly parallel base flow. This base flow being invariant by rotation, all the azimuthal wave numbers are independant, thus the impulse response may be computed independantly for each wave number. In this procedure the axisymmetric flow which correspond to the base flow is kept constant. The computation is done in a sectorial cavity of angular extent $2\pi/\beta$, β being the azimuthal wavenumber whose stability is investigated. At each time step both amplitude ($A_\beta(r,t)$) and phase ($\Phi_\beta(r,t)$) are recorded at every station and defined as:

$$\begin{aligned} A_\beta(r,t) &= r\sqrt{\int_0^{1/2} |\hat{w}^2(r,\beta,z,t)|dz} \\ \Phi_\beta(r,t) &= \arg \hat{w}(r,\beta,z_0,t) \end{aligned}$$

where $\hat{w}(r,\beta,z,t)$ is the spectral coefficient corresponding to azimuthal wave number β, at height z and on the circle of radius r, computed at time t, for the axial velocity taken as the wavepaquet

marker. Figure 2(a) gives an example of such a recording for the amplitude, in a case where the analysed profile is slightly absolutely unstable. The upwing propagation of the trailing edge can already be seen. A more rigorous criteria is obtained when, as in figure 2(b), the logarythm of the amplitude at different time interval t_i is plotted as function of $(r-r_0)/(t_i-t_0)$, r_0 and t_0 being the origin of the perturbation in space and time respectively. The common intersections of the curves mark the edges of a well formed wavepaquet, and the group velocity can be read on the x-axis. Time and space differentiation of A and Φ yields the temporal and spatial growth rates, as well as the absolute frequency. The radial position at which the velocity profile is taken to generate the parallel flow is then varied. When the group velocity of the trailing edge of the wavepaquet vanishes, or equivalently when the growth rate measured at the impulse location is nil, the corresponding parallel flow is marginally absolutely unstable, and the corresponding station marks the limit of the absolutely unstable domain. This approach yielded results fully in agreement with those extrapolated from the single-disk flow analysis by [12] for the position, slope and frequency of the primary front as already shown in the case of a shorter ($L=5$) cavity [2,].

4 Results

The global Reynolds number has been kept constant ($Re_h = 780$) during all the computations, and the mass flow rate has been increased up to the value $C_w = 2500$ which according to a former study must place the transition from convective to absolute instability in the first half of the cavity, and still away from the entry zone. Axisymmetric stationary base flow has been reached through the use of the selective frequency damping, tuned to suppress the type II axisymmetric rolls. The nonlinear dynamics of the flow has been analysed by superimposing an initial spatially localized perturbation during a single time step at the begining of the computations. The perturbation velocity field is a Stokes flow over a hemispherical roughness of radius $R_p/h = 0.008$ located at the wall near the hub. The radius R_p had formerly been shown to be sufficient to induce a nonlinear response of the flow. Azimuthaly periodic perturbations of particular azimuthal wave numbers were achieved by repeating the obstacle at the same radial station a number of time equal to the aimed wavenumber. The impulse response was then monitored by recording the value of the axial velocity for a single azimuth and height ($z = 0.49h$) as a function of radial location and time. Such a data set provides spatiotemporal diagram as shown on figure 4 (a) where the flow asymptotes in time a self-sustained finite amplitude solution evidencing a well-defined upstream front, characteristic of so-alled elephant mode. Characteristics of this nonlinear global mode at the final reported on figure 4(a) are computed by integrating the perturbation kinetic energy as defined in equation 3 and plotting it as a function of the radius (figure 3).

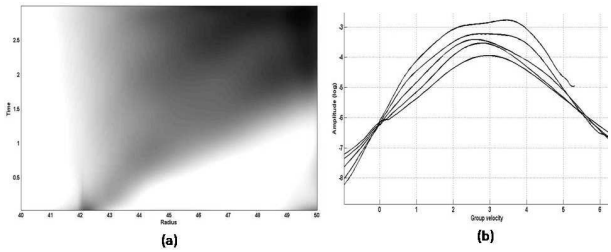

Fig. 2 Spatiotemporal recording corresponding to the impulse response of a parallel base flow made of a velocity profil slightly absolutely unstable. (a) Time evolution of the enveloppe of the wave paquet represented by the axial perturbation velocity. (b) Wavepaquet representation extracted from the data of figure 2(a). The x-axis figures group velocity, and the y-axis is the logarythm of the perturbation amplitude.

$$E(r) = 2\pi r \int_0^{2\pi} \int_{-1/2}^{1/2} \frac{1}{2}(u'^2 + v'^2 + w'^2) dz d\theta \tag{3}$$

(u', v' and w') representing the perturbation velocity with respect to the axisymmetric base flow. From the $E(r)$ profile thus obtained, the position and slope of the front can be precisely de-

termined.

Present results match the predictions of nonlinear global mode theory. The global mode is made of an upstream region where the amplitude of perturbations stays very low compared to the level in the saturated region downstream of the front. Between the two is a front region where the amplitude of the perturbations grows exponentially. This structure is typical of a steep-fronted global mode as described by [15], the so-called elephant mode. The global mode theory predicts that the exponential growth should take place at the station of transition from convective to absolute instability r_{CA}, and that its spatial growth rate should match the local absolute spatial growth rate $k_{0,i}$. In the present computations local analysis yields a position $r_{CA}/h = 24$ for the transition, to be compared with figure 3 where the front is between $r/h = 23.5$ and $r/h = 25$, and a corresponding absolute growth rate $k_{0,i} = 3.41$, in excellent agreement with a measured slope of 3.2. Moreover, analysis of the spiraling arms using gliding FFT to extract a spatial spectrum as a function of the radius, shows that their radial wavelength shifts from $\lambda = 30\delta$ in the upstream part of the front ($r/h \in [23.5;24.5]$) to $\lambda = 18\delta$ in its downstream part ($r/h \in [24.5;26]$). This shift is also visible in the physical space, on figure 4(b). These values are in agreement with [9] study of the type I absolute instability, showing that the value of the absolute mode radial wavelength is $\lambda = 30\delta$ and should shift to $\lambda = 20\delta$, the wave length of the saturated parallel wave beating at the global frequency $\omega_G = \omega_{0,r}(R_{CA})$. And last, the spiraling arms shown on figure 4(b) have a spiral pitch of $\varepsilon = 31°$, to be compared with the theoretically predicted value of $\varepsilon = 30°$. Therefore we can conclude that the nonlinear solution shown in figures 3 and 4(b) is an elephant mode due to the type I absolute instability.

On the spatio-temporal diagram (figure 4(a)) the regular stripes corresponding to the primary spiralling mode are followed, for a r larger than about 26, by scrambled lines. This eratic pattern corresponds to the development of secondary instabilities and it is quite remarkable that their amplitude becomes large enough to scramble the

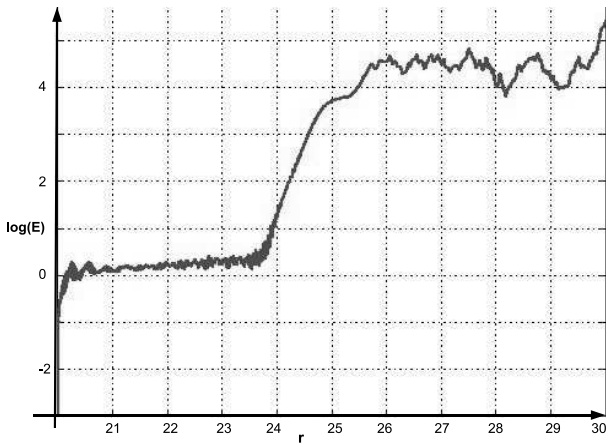

Fig. 3 Log-linear amplitude of the global mode as a function of the radial coordinate, for $C_w = 2500$, $Re_h = 780$ ($Re_\delta \in [330;491]$, $Ro \in [-0.9;-0.45]$).

primary pattern at a well defined steady radius $25.5 < r/h < 26$ downstream of the saturation of the primary wave at $r/h = 25$. This very short interval between the two fronts suggests that the primary saturated wave is already absolutely unstable when it forms. The top view in the physical space, figure 4(b), shows the uniform steady base state at the center, followed by the 68 spiraling arms of the primary global mode, itself giving way to a flow featuring small disorderd scales evoking a turbulent state.

This secondary instability is associated to Floquet number zero, since simulations are conducted in a sectorial cavity of angular extent $2\pi/68$, where only wavenumbers 0, 68 and harmonics are simulated. Moreover, the time at which it appears on figure 4 (a) is exactly the same as the time at which the axisymmetric wave number of the axial velocity in the computational domain stops to be perfectly stationary, as shown on figure 4(c)). And last, the solution in the physical space, filtered to retain only the axisymmetric components, exhibits axisymmetric rolls only downstream of position $r/h = 25.5$, which is approximately the position of the secondary front seen on figure 4(a). It must be noted that the selective frequency damping was kept active in the foremost part of the cavity, prior to the primary

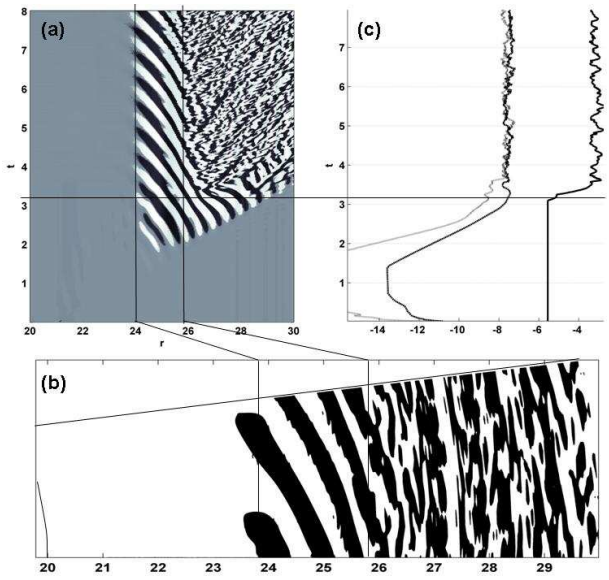

Fig. 4 Impulse response: (a) spatiotemporal recording of the axial velocity for given azimuth $\theta = 0$ and height $z = 0.49$ in the rotating disk boundary layer. Globally unstable flow exhibiting a secondary front ($r \simeq 26$) downwind of the primary ($r \simeq 24$). (b) Thresholding of axial velocity in an horizontal plane, featuring the front between $r = 23.5$ and $r = 25$, the change of radial wavelength from $\lambda = 30\delta$ to $\lambda = 18\delta$ corresponding to the saturation of the type I absolute mode is clearly visible. (c) Time history of the value of the spectral coefficients corresponding to azimuthal wave numbers 0 (rightmost black curve), 68 (middle black curve) and 136 (gray curve) in the whole domain.

front, to make sure that such zero-wavenumber perturbations were not incoming with the inflow, but were locally created. The radial wave length of this secondary rolls has been measured and found equal to $\lambda/\delta = 5.5$, to be compared to the values associated to type I convective, type II convective, and type I absolute instabilities, equal to 13, 22, 29 respectively [2,]. Lastly, computations were carried with the selective frequency damping applied on mode number zero to the whole domain, and the secondary instability was not affected. This tends to prove that its time frequency is much lower than the cutoff ($\omega_c = 1/\Delta = 10$), and consequently much lower than the measured frequencies corresponding to type II axisymmetric instability in this configuration ($\omega = 18$).

This secondary instability leads to a very perturbated state, as seen on figure 4, containing very small scales. These small scales creates a slight aliasing, eventually leading to simulation blow-up, after more than 10 non-dimensionnal time units of rotation. This remains true even though the spatial resolution is quite fine, the order of ten Kolmogorov length scale, showing that at least most of the inertial range is filled. Both the time and radial wavelength spectra become broadband at radius $r/h = 25.5$. Figure 5 shows the three most energetic time frequencies, measured at every radius, extracted from the data of figure 4(a).Using the spectral vanishing viscosity technics of [23] it was possible to prevent aliasing, and the simulation could be continued up to 15 non-dimensionnal time units, to be compared to the 3.5 time units needed to saturates both primary and secondary fronts, and did not exhibit any change in the flow pattern. Therefore we estimate that the flow has reached an equilibrium state, corresponding to the level of turbulence that can be expected close to the transition threshold.

5 Discussion and conclusion

Without artificial damping, numerical noise in the entry zone generates convective axisymmetric rolls. Due to the length of the cavity, they

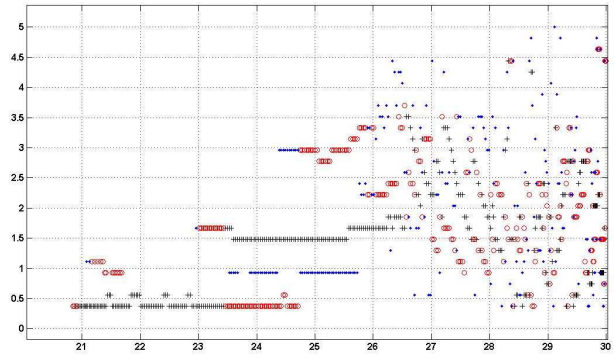

Fig. 5 Time frequencies measured in the data presented on figure 4(a). At every radial station the three most energetic frequencies are plotted using a +, a o and a diamond in decreasing order. Downwind of $r/h = 26$ there is a sudden change in the spectrum.

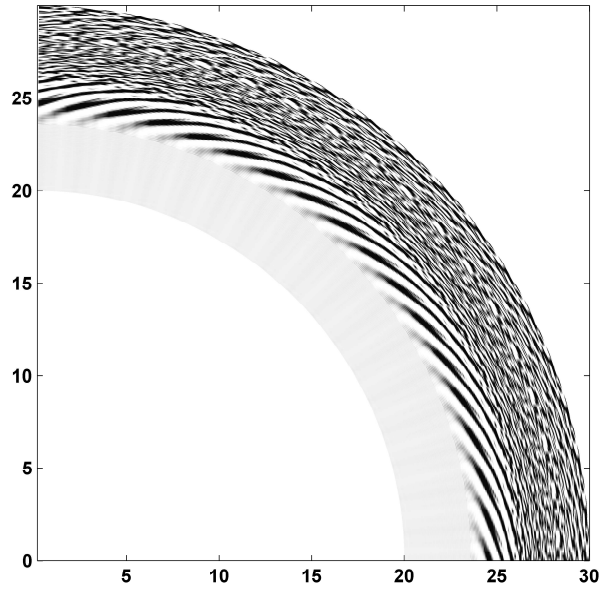

Fig. 6 Iso surfaces of axial velocity in a quarter of cavity, for a given height $z/h = 0.49$ in the rotating disk boundary layer. From the hub to the rim are successive zones of undisturbed flow, spiraling vortices, and turbulent flow.

eventually reach finite amplitude before being advected out of the computational domain, thus modifying the base flow. This modification can be the cause of a change of stability downstream, even to the point of inducing a transition from absolute to convective behaviour. In the case where this A/C transition happens too shortly after the first C/A transition, the absolute zone may be too short to feed the primary front. Results of local analysis have confirmed this scenario, demonstrating the link between un-damped convective rolls, a short absolutely unstable zone, and global convective behaviour. So that further computations have been done using specific frequency damping in the first part of the cavity, priori to the position of the primary front. Such a situation is likely to arise in a natural environment, where the noise level can be expected to be higher than the machine noise in the simulations. In this case the transition scenario may be dominated by convective instabilities, or similar to the one observed in our computations but delayed further downstream, after a second C/A transition.

Computations conducted in a broader cavity, of angular extent $2\pi/4$, and after having introduced a strong secondary perturbation of non-zero azimuthal wavenumber exhibit the same behaviour, they are secondary unstable with Floquet number zero. This tends to show that Floquet number zero is the most unstable, and may hint that having grown first, it forbides the growth of non-zero instabilities, having destroyed their base flow. The top view in the physical space of the resulting flow, seen on figure 6, exhibits the 68 spiraling primary vortices upstream of a highly perturbated area, exactly as in the narrow cavity. But the time history of the spectral coefficients during this computation shows that mode number 1 is rapidly increasing, indicating the breaking of the $2\pi/68$ periodicity.

References

[1] B. Pier and P. Huerre. Nonlinear self-sustained structures and fronts in spatially developping wake flows. *J. Fluid Mech.*, 435:145–174, 2001.

[2] B. Viaud, E. Serre, and J.M. Chomaz. The elephant mode between two rotating disks. *J. Fluid Mech.*, 598:451–464, 2008.

[3] G.K. Batchelor. Note on a class of solutions of the navier–stokes equations representing steady

rotationally-symmetric flow. *Quat.J.Mech. and Appl.Math.*, 4:29–41, 1951.

[4] K. Stewartson. On the flow between two coaxial rotating disks. *Proc.Camb.Phil.Soc.*, 49:333–341, 1953.

[5] R. Hide. On source-sink flows stratified in a rotating annulus. *J. Fluid Mech.*, 32:737–764, 1968.

[6] J.M. Owen and J.R. Pincombe. Velocity-measurements inside a rotating cylindrical cavity with a radial outflow of fluid. *J. Fluid Mech.*, 99:111–127, 1980.

[7] J.M. Owen and R.H. Rogers. *Heat transfer in rotating-disk system*. Wiley, 1995.

[8] C. Davies and P. W. Carpenter. Global behaviour corresponding to the absolute instability of the rotating-disk boundary layer. *J. Fluid Mech.*, 486:287–329, 2003.

[9] B. Pier. Finite amplitude crossflow vortices, secondary instability and transition in the rotating-disk boundary layer. *J. Fluid Mech.*, 487:315–343, 2003.

[10] D. K. Lilly. On the instability of the Ekman layer flow. *J. Atmos. Sc.*, 23:481–494, 1966.

[11] E. Crespo del Arco, E. Serre, P. Bontoux, and B. E. Launder. Stability, transition and turbulence in rotating cavities. In M. RAHMAN, editor, *Advances in Fluid Mechanics*, volume 41 of *Dalhousie University Canada Series*, pages 141–196. WIT press, 2005.

[12] R. J. Lingwood. Absolute instability of the Ekman layer and related rotating flows. *J. Fluid Mech.*, 331:405–428, 1997.

[13] C. Davies, C. Thomas, and P.W. Carpenter. Global stability of the rotating-disk boundary layer. *J. Eng. Math.*, 57:219–236, 2007.

[14] J.M. Chomaz, A. Couairon, and S. Julien. Absolute and convective nature of the Eckhaus and zigzag instability with throughflow. *Phys. of Fluids*, 11:3369–3373, 1999.

[15] B. Pier, P. Huerre, J.M. Chomaz, and A. Couairon. Steep nonlinear global modes in spatially developping media. *Phys. of Fluids*, 10:2433–2435, 1998.

[16] P.J. Zandbergen and D. Dijkstra. Vonkármán swirling flows. *Ann.Rev. Fluid Mech.*, 19:465–491, 1986.

[17] E. Serre, S. Hugues, E. Crespo del Arco, A. Randriamampianina, and P. Bontoux. Axisymmetric and three-dimensional instabilities in an Ekman boundary-layer flow. *Int. J. Heat Fluid Flow*, 22:82–93, 2001.

[18] I. Raspo, S. Hugues, E. Serre, A. Randriamampianina, and P. Bontoux. A spectral projection method for the simulation of complex three-dimensional rotating flows. *Comput. fluids*, 31:745–767, 2002.

[19] J. M. Vanel, R. Peyret, and P. Bontoux. A pseudo-spectral solution of vorticity-streamfunction equations using the influence matrix technic. In K. W. Morton and M. J. Baynes, editors, *Num. Meth. for fluid dynamics*, volume II, pages 463–475. 1986.

[20] E. Crespo del Arco, P. Maubert, A. Randriamampianina, and P. Bontoux. Spatio-temporal behaviour in a rotating annulus with a source-sink flow. *J. Fluid Mech.*, 32:1–27, 1996.

[21] E. Akervik, L. Brandt, D.S. Henningson, and J. Hoepffner. Steady solutions of the navier–stokes equations by selective frequency damping. *Phys. Fluids*, 18:126602, 2006.

[22] Y. Delbende, J.M. Chomaz, and P. Huerre. Absolute/convective instabilities in the batchelor vortex: a numerical study of the linear impulse response. *J. Fluid Mech.*, 355:229–254, 1998.

[23] E. Severac and E. Serre. A spectral vanishing viscosity for the les of turbulent flows within rotating cavities. *J. Comput. Phys.*, 226:1234–1255, 2007.

Copyright Statement